RASĀYAN *J. Chem.*
Vol. 18 | No. 2 |842-849| April - June | 2025
ISSN: 0974-1496 | e-ISSN: 0976-0083 | CODEN: RJCABP
http://www.rasayanjournal.com
http://www.rasayanjournal.co.in

STRUCTURE, MAGNETIC PROPERTIES, AND PHOTOCATALYTIC PERFORMANCE OF SOL-GEL DERIVED $Nd_{0.70}Ca_{0.30}MnO_3$ PEROVSKITE NANOPARTICLES: A NOVEL CATALYST FOR ENVIRONMENTAL APPLICATIONS

Bhupendra Singh[1], Gaurav Joshi[2], Hira Ilyas[2], Sudha Tomar[2] and Lalit Kumar[3,✉]

[1]Department of Physics, Ch. Chhotu Ram (P.G.) College, Muzaffarnagar, India, 251001
[2]Department of Applied Science and Humanities, Invertis University Bareilly, India, 243006
[3]Department of Physics, Meerut College Meerut, India, 250001
✉Corresponding author: lalitksuvaksh@gmail.com

ABSTRACT

Sol-gel synthesized $Nd_{0.70}Ca_{0.30}MnO_3$ nanoparticles were examined for their structural, magnetic, and photocatalytic characteristics. X-ray diffraction analysis was used to establish the phase purity and structural features; Rietveld refinement revealed an orthorhombic crystal structure inside the Pnma space group. The lattice constants reveal a typical O sub-type orthorhombic pattern influenced by the Jahn-Teller effect, with an average crystallite size of 18 nm. Field emission scanning electron microscopy and transmission electron microscopy images showed uniform particle distribution with coarse surfaces, confirming a nanoscale morphology with an average particle size of 85 nm. Energy dispersive X-ray spectroscopy affirmed the intended elemental composition of Nd, Ca, Mn, and O. Magnetic measurements demonstrated temperature-dependent irreversibility in zero-field-cooled and field-cooled-warming modes, with hysteresis attributed to coexisting ferromagnetic and antiferromagnetic interactions, suggesting a cluster glass-like state. X-ray photoemission spectroscopy revealed mixed Mn oxidation states (Mn^{3+}/Mn^{4+}), affecting magnetic ordering through Mn-O-Mn bond variation. The photocatalytic activity was evaluated through the degradation of Eriochrome Black T dye under sunlight, achieving 67.5% degradation within 60 minutes, following pseudo-first-order kinetics with a rate constant of 0.01975 min^{-1}. This study provides insights into the potential of $Nd_{0.70}Ca_{0.30}MnO_3$ as a multifunctional material for catalytic and magnetic applications.

Keywords: Rietveld Refinement, Sol-Gel, Manganite, Eriochrome Black T, Antiferromagnetic.

RASĀYAN*J. Chem.*, Vol. 18, No.2, 2025

INTRODUCTION

Nanoscale materials, such as nanoparticles, nanowires, nanotubes, and nanocomposites, are currently at the forefront of research due to their unique physical properties and potential for groundbreaking technological applications across various fields, including logic circuits, magneto-electronic devices, magnetic data storage, biotechnology, and medicine.[1–4]These applications are driven by nanoscale phenomena such as improved surface-to-volume ratios, interface effects, and quantum confinement effects.These offer exceptional possibilities for manipulating size to adjust material behavior. Strong correlations between spin, electron, and orbital degrees of freedom have influenced the complex magnetic and electronic behaviors of perovskite manganites, which have a standard formula $R_{1-x}A_xMnO_3$ (where R is a rare earth ion and A is an alkaline earth ion). These behaviors include colossal magnetoresistance (CMR), charge ordering (CO), orbital ordering (OO), and separation of phases.[5–8]The properties of these manganites are susceptible to factors like composition, temperature, and external electric or magnetic fields. Particularly intriguing are the effects of size reduction, which can dramatically alter phase transitions.[9,10] For instance, the transition temperature (Tc) from a semiconducting paramagnetic state to a metallic ferromagnetic (FM) state in CMR compounds may shift when the material is synthesized at the nanoscale. The suppression of CO and antiferromagnetic (AFM) phases, along with the emergence of ferromagnetism, has been demonstrated in nanostructures such as nanowires of $Pr_{0.5}Ca_{0.5}MnO_3$[11,12], and similar effects are observed in nanoparticles of $Nd_{0.5}Ca_{0.5}MnO_3$.[3,13]In particular, the electron-doped manganites $Ln_xCa_{1-x}MnO_3$, where $x < 0.5$, exhibit remarkable behaviors compared to their hole-doped

http://doi.org/10.31788/RJC.2025.1829153

counterparts. These compositions, characterized by antiferromagnetic ground states, are dominated by charge ordering, with phase separation phenomena playing a key role in their magnetic and electronic properties.[9,14]For example, studies on the $Ln_{0.57}Ca_{0.43}MnO_3$ system[15], doped with Ba, have revealed a predisposition towards ferromagnetism even in the absence of external magnetic fields, further demonstrating the profound impact of compositional tuning on these complex oxides.The nanoscale exploration of rare-earth manganites offers valuable insights into phase separation and the electronic properties resulting from reduced dimensions. It has been shown that downsizing these materials to nanostructures weakens the CO-OO and antiferromagnetic orders, reducing the critical magnetic fields required to disrupt them. This size reduction also leads to the emergence of exchange bias behaviors, cluster glass states, and the substitution of antiferromagnetic phases with disordered ferromagnetic phases, further altering the material's properties at low temperatures.[16–19]ABO_3 perovskite structures typically feature a smaller transition metal ion at the octahedral site (B site), while a larger cation, often a rare earth, alkaline earth, or alkali metal, occupies the A site and is surrounded by 12 oxide ions. The Mn^{3+}/Mn^{4+} redox pair in perovskites such as $LaMnO_3$ enables reversible reduction and is particularly beneficial for heterogeneous catalysis applications. While extensive research has focused on the photocatalytic activity of $LaMnO_3$ under illumination, its catalytic performance without a light source remains less explored. For instance, researchers synthesized $LaMnO_3$ nanoparticles using the complex sol-gel method and demonstrated their efficiency in Rhodamine B (RhB) degradation under acidic conditions (pH ~1), attributing the activity to the Mn^{3+}/Mn^{4+} redox cycling. Additionally, Sharma et al. investigated $La_{0.5}A_{0.5}Mn_{0.5}Fe_{0.5}O_3$ (A = Sr, Ca) nanoparticles for degrading organic dyes and found that Sr-doped samples achieved 99% degradation within 25 minutes. This enhanced performance was attributed to the Mn^{3+}/Mn^{4+} redox mechanism and the larger surface area of the Sr-doped material.[20–23] In this study, we explore the structural, magnetic, catalytic, and electric transport properties of sol-gel derived $Nd_{0.70}Ca_{0.30}MnO_3$ (NCM). The primary objective is to understand how the unique properties of this material evolve with size reduction and compositional variations, with a particular focus on the influence of nanoscale effects on magnetism, charge ordering, and overall phase behavior. Additionally, we investigate the potential of NCM as a photocatalyst for the degradation of Eriochrome Black T (EBT) dye, analyzing the rate constant and reaction order to better understand its catalytic efficiency. Our investigation aims to contribute to the broader understanding of how nanostructuring and chemical modifications can be harnessed to tune the properties of perovskite manganites for practical applications in magnetic memories, and environmental remediation.

EXPERIMENTAL

A nanocrystalline sample with the nominal composition of $Nd_{0.70}Ca_{0.30}MnO_3$ (NCM) was synthesized using a conventional polymeric sol-gel process. First, high-purity nitrates of Nd, Ca, and Mn were weighed in stoichiometric proportions and dissolved in distilled water at room temperature, forming a homogeneous aqueous solution. Ethylene glycol was then added in equal quantities, and the mixture was stirred continuously to ensure thorough blending. This solution was subsequently heated on a hot plate at a temperature range of 80–100 °C, converting into a thick brown sol. The brown sol was dried in an oven at around 300 °C for 4 hours, yielding a fluffy, dry material. After grinding, this material was calcined at 400 °C for 12 hours. The calcined powder was then reground, pelletized, and sintered at 900 °C for 5 hours to obtain the final NCM sample.The Debye–Scherrer equation provided valuable insights into the nanocrystalline nature of the synthesized material and was used to determine the average crystallite size (t) for the NCMO sample.

$$t = \frac{K\lambda}{\beta\cos\theta} \qquad (1)$$

Here, K= 0.9 (Scherrer constant), $\lambda = 1.54$ (wavelength of X-ray), $\beta =$ Full width at half maxima (FWHM) The structural properties of the NCM sample were analyzed using a powder X-ray diffractometer (Rigaku, Cu Kα radiation, λ = 1.5418 Å). The sample was scanned at a rate of 1°/min, covering a 2θ range from 20° to 80°. Rietveld refinement was applied to the XRD data for precise structural characterization. The morphology of the NCM sample was meticulously analyzed using a Carl Zeiss Ultra scanning electron microscope, which enabled a detailed examination of the surface characteristics of the nanoparticles. Complementary to this, the elemental composition of the NCM

sample was determined through Energy-Dispersive Spectroscopy (EDS), providing valuable information on the distribution of elements within the sample. Furthermore, the magnetic properties of the NCM nanoparticles were systematically studied under magnetic fields up to 2 T using a VSM (Vibrating Sample Magnetometer). The photocatalytic degradation performance of the NCM catalyst was evaluated using Eriochrome Black T dye as a model pollutant. In a typical experiment, 20 mg of the catalyst was dispersed in 60 mL of a 5 ppm dye solution and stirred for 30 minutes in the dark to establish adsorption/desorption equilibrium. Following this, the mixture was exposed to natural sunlight to initiate the photocatalytic reaction. At fixed time intervals, 3 mL aliquots were withdrawn, and centrifuged, and the absorbance of the supernatant was measured using UV-Vis spectroscopy at the maximum absorption wavelength of the dye ($\lambda_{max} \approx 530$ nm). The percentage of dye degradation was calculated using the equation: Degradation (%) = $[(C_0 - C) / C_0] \times 100$, where C_0 is the initial concentration of the dye, and C is the concentration at a specific time point.

RESULTS AND DISCUSSION

Structural Properties

The phase purity of the synthesized NCM sample was confirmed using powder X-ray diffraction (XRD) analysis. The collected XRD data underwent Rietveld refinement via the FullProf software, revealing that the sample aligns best with an orthorhombic crystal structure in the ***Pnma*** space group. Figure 1 illustrates both the observed and calculated XRD patterns, showing a close match that affirms the sample's crystallization in this specific orthorhombic structure. Structural parameters (a, b, c) obtained from the Rietveld refinement are listed in Table-1. In the NCM perovskite structure, Mn ions occupy the B site, surrounded by oxygen octahedra that form a connected three-dimensional network by sharing corners. The A sites, positioned between the MnO_6 octahedra, are occupied by Nd/Ca ions. The lattice parameters display a characteristic pattern with $a > c > b/\sqrt{2}$, indicating an O' subtype orthorhombic structure, influenced by the Jahn-Teller effect.[24,25]This effect causes distortions in the MnO_6 octahedra, which exhibit bond length anisotropy due to one Mn-O1 bond pair and two Mn-O2 bond pairs of varying lengths. This variation in bond lengths induces a pronounced Jahn-Teller distortion in the MnO_6 octahedra. Additionally, the average crystallite size (Dc) of the NCM sample, calculated using Scherrer's equation, is approximately 18 nm.

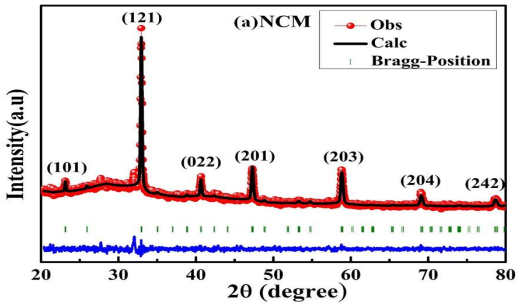

Fig.-1: Rietveld Refinement Pattern of NCM Sample

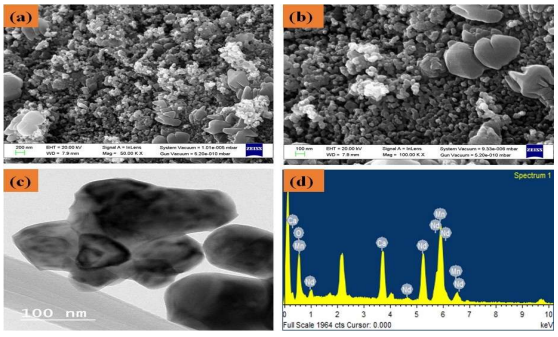

Fig.-2: (a), and (b) Show the FESEM Images of NCM at different Scales, (c) Show the TEM Image of NCM at 100 nm Scale and (d) Representative EDS of NCM Sample.

Figure-2 (a, b, c, and d) shows the microstructural and elemental composition analysis of sol-gel derived $Nd_{0.70}Ca_{0.30}MnO_3$ (NCM) nanoparticles. Images (a) and (b) are SEM images at different magnifications, which reveal a relatively uniform distribution of NCM particles with irregular shapes. The particles exhibit a coarse surface texture with agglomerates, indicating a nano-grain morphology. The average particle size is approximately 85 nm, confirming the nanoscale nature of the synthesized material. Image (c) is a TEM image, providing a closer look at individual NCM nanoparticles, which appear as clustered aggregates with some degree of porosity. The nanoscale structure is evident, supporting high surface area, which is advantageous for catalytic applications. Image (d) is an EDX spectrum confirming the elemental composition of the NCM nanoparticles, showing prominent peaks for Nd, Ca, Mn, and O, indicating the successful incorporation of these elements into the perovskite structure. The presence of these elements supports the anticipated stoichiometry of the $Nd_{0.70}Ca_{0.30}MnO_3$ composition. Table-1Shows the Microstructural and structural parameters infested through XRD and FE-SEM.

Table-1: Microstructural and Structural Parameters Infested Through XRD and FE-SEM

Sample	NCM
a(Å)	5.432
b(Å)	7.680
c(Å)	5.428
Mn-O1-Mn (Å)	1.939
Mn-O2-Mn (Å)	1.962
Mn-O2-Mn (Å)	1.929
⟨Mn-O⟩ (Å)	1.950
Mn-O1-Mn (deg)	157.95
Crystallite Size (CS) nm	18
Particle Size (PS) nm	85

Magnetic Properties

By evaluating magnetization as a function of temperature and magnetic field, the magnetic characteristics of $Nd_{0.70}Ca_{0.30}MnO_3$ have been investigated. Measurements of temperature-dependent magnetization (M-T) in zero-field cooling (ZFC), field-cooled cooling (FCC), and field-cooled warming (FCW) modes were carried out at a magnetic field of H=100 Oe. In Fig.-3, the magnetization data is displayed. The data was gathered during the heating cycle in ZFC while the sample was chilled from 300 K down to 10 K with no magnetic field present. Data has been recorded down to 10 K during the FCC cycle when the sample is cooling in the vicinity of a magnetic field, and up to 300 K during the FCW cycle when the sample is warming to ambient temperature while a magnetic field is maintained. The ZFC and FCW curves exhibit significant irreversibility, the FCC or FCW curve exhibits hysteresis, the FCC and FCW exhibit reversible behavior in the lower temp region, and the ZFC Cycle shows a quick decline in the low-temperature zone, according to the M-T data in Fig.-3a.

The characteristic hallmark of phase separation caused by a combination of FM and AFM orders is ZFC-FCW irreversibility, which is typically distinct from that of the delegate's spin glass phase and similar to cluster glass.[26–28]The supercooling of a liquid-like magnetic equilibrium due to the magnetic irritation by conflicting FM and AFM-CO engagement is thought to be the source of the noticeable hysteresis among FCC and FCW arcs in M-T plots.[26,27,29–33]The area of the loop is discovered to be 33.47. The greater the FCC-FCW enclosed area, the more sensitive the balance within the FM and AFM phases, and hence the stronger the hysteresis. The ZFC magnetization exhibits a synchronous decline in the lowest temperature zone, while the FCC and FCW arcs exhibit irreversible behavior. The emergence of a spin glass-like state may give birth to such properties. In the sample, the ZFC decrease and FCC-FCW irreversibility happen at T_C~33 K. It is determined that T_f ~ 41 K is the temperature where the FCC or FCW arcs seem to saturate. As the temperature drops, the FCC M-T reaches saturation, indicating that the moments are freezing, While the FCW curve shows the wider thermal span across which the moment freezing persists, the FCC M-T saturation indicates the freezing of the moments when the temperature is dropped.For more information about the magnetic behavior, the temperature dependence of the inverse magnetic susceptibility [χ^{-1}(T)] has been plotted using the ZFC data of the sample and shown in fig.3 (b). At high-temperature regions, χ^{-1} vs. T curve accompanies Curie-Weiss law:

$$\chi(T) = \frac{C}{T-\Theta} \quad (2)$$

Where C is the Curie constant and Θ is Curie-Weiss temperature.

The value of C is found to be close to 98.46 when the data is fitted using the Curie-Weiss equation in the paramagnetic zone. At various temperatures, the magnetization against magnetic field (M-H) data has been gathered.Figure-3 (c, d) displays the (M-H) values for the sample that were obtained at 20 K and 300 K. After cooling the specimen at room temperature without the use of a magnetic field, the M-H data at 20 K was obtained. Sample does not exhibit clear magnetization saturation beyond H = 20 kOe, according to the results at 20 K. This suggests that there is an AFM component in the sample. M-H curves at 300 K show that every sample behaves as though it were paramagnetic.

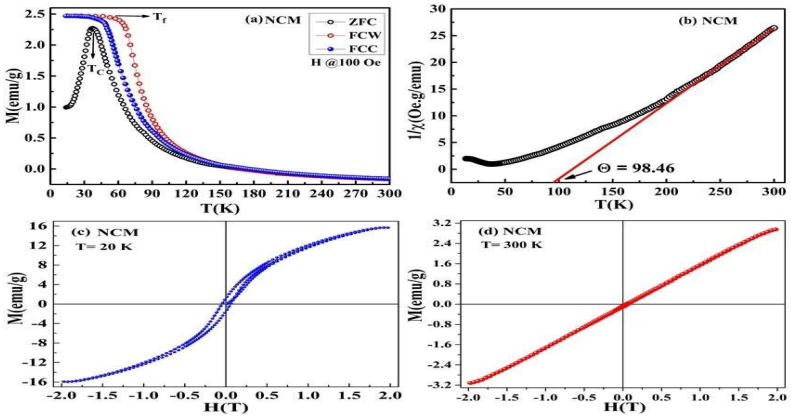

Fig.-3:(a) Magnetization Against Temperature (M-T) Curves for Zero-Field-Cooled (ZFC), Field-Cooled Cooling (FCC), and Field-Cooled Warming (FCW) at 100 Oe Magnetic Field; (b) 1/Chi vs. Temperature; and (c, d) Hysteretic Curves for Magnetic Field Against Magnetization (M-H) at 20 K and 300 K for the NCM Sample

X-Ray Photoemission Spectroscopy

In this study, X-ray photoemission spectroscopy (XPS) was employed to investigate the oxidation state of the Mn element in the NCMO sample. XPS proved especially useful for determining the proportion of Mn ions in different oxidation states (Mn^{3+} and Mn^{4+}), thus validating the actual composition of divalent cations. Analysis of the Mn (2p) spectra revealed the presence of both Mn^{3+} and Mn^{4+}, indicating mixed oxidation states that significantly affect the local Mn-O-Mn bonding environment and, consequently, influence magnetic ordering within the system. The Mn2p core level spectra displayed centered binding energies at 641.7 eV for $Mn2p_{3/2}$ and 652.8 eV for $Mn2p_{1/2}$, with a spin-orbit splitting of around 12 eV. This separation aligns with the expected energies for Mn in the +3 and +4 valence states, as well as their mixed state.[14]Fitting analysis of the Mn2p region allowed for deconvolution of the peaks, corresponding to Mn^{3+} and Mn^{4+}, as shown in Fig.-4.

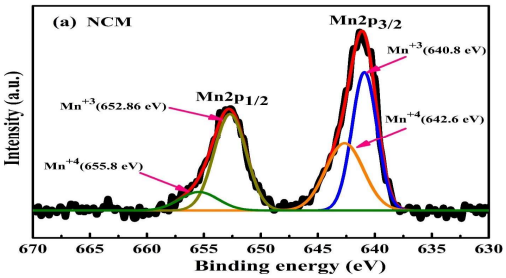

Fig.-4: Represents Mn2p X-Ray Photoemission Spectra for the NCM Sample

Photocatalytic Degradation of Dye

The photocatalytic degradation of Eriochrome Black T dye under sunlight irradiation was evaluated using $Nd_{0.70}Ca_{0.30}MnO_3$ catalyst in Fig.-5. The degradation efficiency was observed concerning time and a significant decrease in the intensity of the absorption peak at 530 nm was noted, indicating progressive dye breakdown. Complete degradation occurred after 60 minutes of irradiation. The photocatalytic

degradation followed pseudo-first-order reaction kinetics, described by the equation $\ln(C/C_0) = -k_1t$, where k_1 is the rate constant. The reaction rate constant k_1 was calculated as 0.01975 min^{-1}, and 67.5% of the dye was degraded within 60 minutes of sunlight exposure.[21–23,34–37]

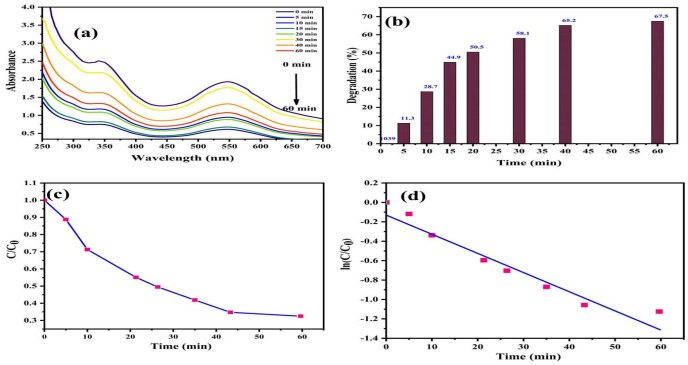

Fig.-5: Dye Degradation Study: (a) UV-vis Graphs of Eriochrome Black T (EBT) Dye in a Time-Bound Study, (b) Dye Removal Efficiency with Reaction Time (c, d) Kinetic Study of Dye Degradation

CONCLUSION

In this study, we synthesized and characterized $Nd_{0.70}Ca_{0.30}MnO_3$ (NCM) nanoparticles, confirming phase purity and structural integrity via X-ray diffraction (XRD) analysis and Rietveld refinement, which identified an orthorhombic crystal structure in the Pnma space group. The microstructural properties, examined through FESEM and TEM, revealed nanoscale particles with a coarse surface texture and irregular shapes, with an average crystallite size of 18 nm and particle size of approximately 85 nm. Elemental composition analysis by EDS confirmed the incorporation of Nd, Ca, Mn, and O, aligning with the expected stoichiometry of NCM. Magnetic properties were assessed by magnetization measurements as a function of temperature and magnetic field, revealing complex behavior attributed to competing ferromagnetic (FM) and antiferromagnetic (AFM) interactions. Zero-field-cooled (ZFC) and field-cooled (FCC/FCW) magnetization curves indicated large irreversibility and hysteresis, suggesting a cluster glass state and phase separation between FM and AFM orders. The temperature dependence of inverse susceptibility followed Curie-Weiss law in the high-temperature region, providing the Curie constant and confirming the paramagnetic nature of NCM at room temperature. Magnetic hysteresis loops measured at 20 K and 300 K further confirmed the presence of AFM and paramagnetic components. X-ray photoemission spectroscopy (XPS) of the Mn (2p) core levels revealed mixed oxidation states (Mn^{3+}/Mn^{4+}) in the NCM sample, with characteristic binding energies, confirming the role of Mn valence states in influencing local Mn-O-Mn bonding and magnetic ordering. Finally, the photocatalytic performance of the NCM catalyst was evaluated by the degradation of Eriochrome Black T dye under sunlight. The catalyst achieved 67.5% dye degradation within 60 minutes, following pseudo-first-order kinetics with a rate constant of 0.01975 min^{-1}. The study highlights the potential of $Nd_{0.70}Ca_{0.30}MnO_3$ as a multifunctional material with applications in magnetic and photocatalytic systems.

ACKNOWLEDGMENTS

The XRD, FESEM, and VSM facilities provided by IIT Roorkee are for which the authors are grateful. The UV-Vis, spectrometers were provided by Invertis University Bareilly. The authors also express their gratitude to these organizations.

CONFLICT OF INTERESTS

The authors declare that there is no conflict of interest.

AUTHOR CONTRIBUTIONS

All the authors contributed significantly to this manuscript, participated in reviewing/editing and approved the final draft for publication. The research profile of the authors can be verified from their ORCID ids, given below:

Bhupendra Kumar https://orcid.org/0009-0006-2558-776X
Gaurav Joshi https://orcid.org/0009-0001-7234-3454

Hira Ilyas https://orcid.org/0009-0007-4795-6615
Sudha Tomar https://orcid.org/0000-0002-1219-133X
Lalit Kumar https://orcid.org/0009-0005-0540-6071

REFERENCES

1. P. H. Hoet, I. Brüske-Hohlfeld, and O. V. Salata, *Journal of Nanobiotechnology*, **2(1),** 115(2004), https://doi.org/10.1186/1477-3155-2-12.
2. P. R. Bandaru, C. Daraio, S. Jin, and A. M. Rao, *Nat. Mater*, **4(9)**, 663(2005), https://doi.org/10.1038/nmat1450.
3. F. Millange, S. De Brion, and G. Chouteau, *Physical Review. B, Condensed Matter***, 62(9)**, 5619(2000), https://doi.org/10.1103/PhysRevB.62.5619.
4. A. Fert and L. Piraux, *Journal of Magnetism and Magnetic Materials*, **200(1–3)**, 338(1999), https://doi.org/10.1016/S0304-8853(99)00375-3.
5. H.S. Im, G.B. Chon,S.M. Lee, B.H. Koo, C.G. Lee and M.H. Jung, *Journal of Magnetism and Magnetic Materials*, **310(2)**, 2668(2007), https://doi.org/10.1016/j.jmmm.2006.12.002.
6. H.Bhatt, Y. Kumar, C.L. Prajapati, S.D. Kaushik, S. Basu and S. Singh, *Journal of Magnetism and Magnetic Materials*, **485**, 118(2019), https://doi.org/10.1016/j.jmmm.2019.04.046.
7. Y. Tokura, *Reports on Progress in Physics*, **69(3)**, 797(2006), https://doi.org/10.1088/0034-4885/69/3/R06
8. Q. H. Lu, K. L. Yao, D. Xi, Z. L. Liu, X. P. Luo, and Q. Ning, *Journal of Magnetism and Magnetic Materials*, **301(1)**, 44(2006), https://doi.org/10.1016/j.jmmm.2005.06.007
9. H. Yang, Y.H. Zhu, T. Xian and J.L. Jiang, *Journal of Alloys and Compounds*, **555**, 150(2013), https://doi.org/10.1016/j.jallcom.2012.11.200
10. R. Prasad, M.P. Singh, P.K. Siwach, P. Fournier and H.K. Singh, *EPL (Europhysics Letters)*, **84(2)**, 27003(2008), https://doi.org/10.1209/0295-5075/84/27003.
11. S. Hébert, A. Maignan, C. Martin and B. Raveau, *Solid State Communications*, **121(5)**, 229(2002), https://doi.org/10.1016/S0038-1098(01)00513-0
12. V. Agarwal, R. Prasad, M.P. Singh, P.K. Siwach and A. Srivastava, *Applied Physics Letters*, **96(5)**, 052512(2010), https://doi.org/10.1063/1.3302455
13. H. Kawano, R. Kajimoto, H. Yoshizawa, Y. Tomioka, H. Kuwahara, and Y. Tokura, *Physical Review Letters*, **78(22)**, 4253(1997), https://doi.org/10.1103/PhysRevLett.78.4253.
14. E. Beyreuther, S. Grafström, L.M. Eng, C. Thiele and K. Dörr, *Physical Review B*, **73 (15),** 155425(2006), https://doi.org/10.1103/PhysRevB.73.155425.
15. T.L. Phan, T.A. Ho, T.V. Manh, N.T. Dang C.U. Jung, B.W. Lee and T.D. Thanh, *Journal of Applied Physics*, **118(14),** 143902(2015), https://doi.org/10.1063/1.4933179.
16. E.O. Wollan and W.C. Koehler, *Physical Review*, **100(2),** 545(1955), https://doi.org/10.1103/PhysRev.100.545.
17. I.O. Troyanchuk, D.D. Khalyavin, S.V. Trukhanov and H. Szymczak, *Journal of Physics Condensed Matter***, 11 (44)**, 8707(1999), https://doi.org/10.1088/0953-8984/11/44/309.
18. N. Furukawa, *Journal of the Physical Society of Japan*, **64(9)**, 3164(1995), https://doi.org/10.1143/JPSJ.64.3164.
19. Y. Murakami, J.P. Hill, D. Gibbs, M. Blume, I. Koyama, M. Tanaka, H. Kawata, T. Arima, Y. Tokura, K. Hirota and Y. Endoh, *Physical Review Letters*, **81(3),** 582(1998), https://doi.org/10.1103/PhysRevLett.81.582.
20. S. Singh, N.D. Sharma, M.K. Verma, R. Singh and D. Singh, *ChemistrySelect*, **9(28),** 2024, https://doi.org/10.1002/slct.202400092.
21. E. V. Nascimento, A.M. Garrido Pedros and M.J.B. Souza, *Water Science & Technology***, 83(11),** 2793(2021), https://doi.org/10.2166/wst.2021.174.

22. S. Sagadevan,R.P. Sivasankaran, J. A. Lett, I. Fatimah, G. K. Weldegebrieal, E. Léonard, M. V. Le and T. Soga, *Symmetry (Basel)*, **15(6),**1139(2023), https://doi.org/10.3390/sym15061139.
23. H. Tavakkoli and T. Moayedipour *Journal of Nanostructure in Chemistry*, **4(3)** 2014, https://doi.org/10.1007/s40097-014-0116-z.
24. A. P. Ramirez, *Journal of Physics Condensed Matter*, **9(39),** 8171(1997), https://doi.org/10.1088/0953-8984/9/39/005.
25. J. A. Collado, C. Frontera, J. L. García-Muñoz,C. Ritter, M. Brunelli and M.A.G. Aranda, *Chemistry of Materials*, **15(1),** 167(2002), https://doi.org/10.1021/cm020776u.
26. V. Podzorov, B. G. Kim, V. Kiryukhin, M. E. Gershenson, and S. Cheong, *Physical Review. B, Condensed Matter*, **64(14)**, 140406(2001), https://doi.org/10.1103/PhysRevB.64.140406.
27. P. A. Sharma, S. B. Kim, T. Y. Koo, S. Guha, and S. Cheong, *Physical Review B*, **71(22),** 224416(2005), https://doi.org/10.1103/PhysRevB.71.224416.
28. W. Wu, C. Israel, N. Hur, S. Park, S.-W. Cheong, and A. De Lozanne, *Nature Materials*, **5(11),** 881(2006), https://doi.org/10.1038/nmat1743.
29. L. Ghivelder, and F. Parisi, *Physical Review B*, **71(18),** 184425(2005), https://doi.org/10.1103/PhysRevB.71.184425.
30. T. Dhakal, J. Tosado and A. Biswas, *Physical Review B*, **75(9)**, 092404(2007), https://doi.org/10.1103/PhysRevB.75.092404.
31. T. Z. Ward, S. Liang, K. Fuchigami, L. F. Yin, E. Dagotto, E. W. Plummer and J. Shen, *Physical Review Letters*, **100(24),** 247204(2008), https://doi.org/10.1103/PhysRevLett.100.247204.
32. D. Gillaspie, J.X. Ma, H.-Y. Zhai, T. Z. Ward, H.M. Christen, E. W. Plummer and J. Shen, *Journal of Applied Physics*, **99(8),** 08S901(2006),https://doi.org/10.1063/1.2162050.
33. M. Uehara, S. Mori, C. H. Chen and S.-W. Cheong, *Nature*, **399(6736)**, 560(1999),https://doi.org/10.1038/21142.
34. I. Qadir, S. Singh, S. Sharma, U. Manhas, A. K. Atri and D. Singh, *ACS Omega*, **8(2)**, 2010(2023),https://doi.org/10.1021/acsomega.2c05221.
35. A. A. Kalicharan, N. A. Kistan, N. S. Jothilakshmi, N. S. Rekha, and N. S. Mohan, *Rasayan Journal of Chemistry*, **17(04),** 1416(2024), https://doi.org/10.31788/rjc.2024.1748906.
36. S. M. Khetre, H. V. Jadhav and S. R. Bamane, *Rasayan Journal of Chemistry*, **2(1),** 174(2009).
37. N. P. Raja, M. Taj, K. C. Kumar, and N. S. Gowrishankar, *Rasayan Journal of Chemistry*, **17(04)**, 1401(2024), https://doi.org/10.31788/rjc.2024.1748943.

[RJC-9153/2024]